Supplementary Information: Electronic Modulation of Near Field Radiative Transfer in Graphene Field Effect Heterostructures

Nathan H. Thomas,[1] Michelle C. Sherrott,[2,3] Jeremy Broulliet,[3] Harry A. Atwater,[4,3] and Austin J. Minnich[1,*]

[1] *Division of Engineering and Applied Science, California Institute of Technology, Pasadena, California 91125, United States*

[2] *Current Address: Research Laboratory of Electronics, Massachusetts Institute of Technology, Cambridge, MA, 02139*

[3] *Thomas J. Watson Laboratory of Applied Physics*

[4] *Resnick Sustainability Institute, California Institute of Technology, Pasadena, California 91125, United States*

[*] aminnich@caltech.edu

S1. SAMPLE SCHEMATIC

A diagram of the sample is shown in Figure S1. The temperatures T_1 and T_2 are recorded with K type thermocouples, embedded in copper heat spreaders above and below the samples. The top and bottom samples are separated by SiO_2 posts fabricated by electron beam lithography and subsequent electron beam deposition.

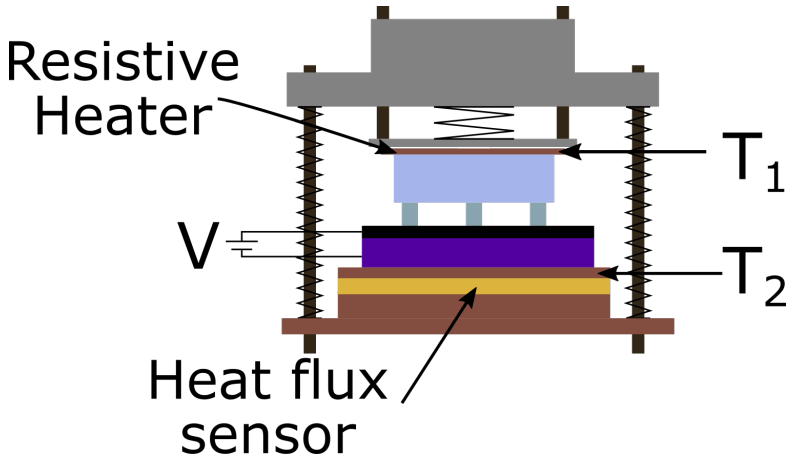

FIG. S1. **Diagram of experimental setup.** The top and bottom samples are separated by posts of SiO_2. To measure T_1 and T_2, the thermocouples are embedded in copper heat spreader plates.

S2. WET TRANSFER OF CVD GRAPHENE

The graphene used in these experiments is grown by chemical vapor deposition on copper foil. The samples in these experiments are quite large, 15 mm × 20 mm. For standard wet transfer techniques typically, once the copper foil has been etched away, the floating graphene must be transferred to a series of water baths. We find that the samples here were large enough that they often tore during the transfer from bath to bath. To overcome this problem, the transfer method shown in Figure S2 was developed. The copper foil is etched

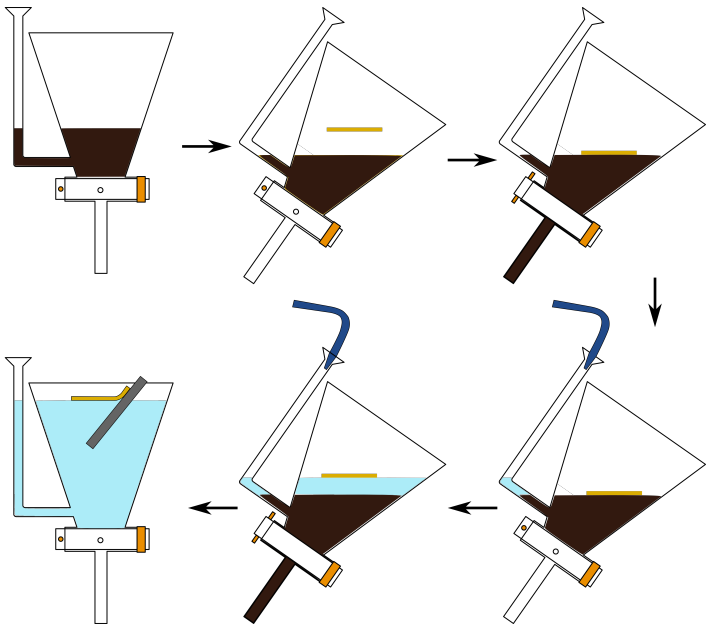

FIG. S2. **Modified wet transfer technique.** The copper foil upon which the graphene was grown is etched in a modified seperatory funnel. Instead of removing the graphene from the etchant to be cleaned, the etchant is removed by opening the stopcock and then displaced with de-ionized water.

in a modified separatory funnel with additional snorkel welded above the stopcock. Once the copper is completely etched, the stopcock is slowly opened and etchant drips out the bottom of the funnel, while it is being displaced with de-ionized (DI) water, poured through the snorkel. The DI water is added repeatedly until the etchant has been completely washed away, and the graphene is sufficiently clean. Then the graphene is picked up by a sample substrate.

The sample substrates undergo a rigorous cleaning process. First, they are sonicated in isopropyl alchohol for 15 minutes, after which they are dried and cleaned in an O_2 plasma

clean for 60 minutes. Finally, to prepare the substrate surface for graphene transfer, the substrates are soaked in a pirahna solution overnight.

S3. HEAT FLUX SENSOR CALIBRATION

The heat flux sensor is a critical component to the apparatus. The signal response for a given thermal input is dependent on the sample temperature and requires careful calibration. We calibrate the sensor at 5 temperatures from room temperature down to 90 K. First, the heating element is pressed directly onto the copper heat spreader with thermal grease applied to both. The heater is held in place with two actuator screws. To limit conductive loss through the screws, low thermal conductivity ceramic washers and a glass spacer separate the screw from the aluminum shroud that encompasses the heater (see Section S4).

The heat flux sensor signal in μV was tracked in time at the given input powers into the heater, as shown in Figure S3. After the input power and heat flux signal have equilibrated, the average input power and sensor voltage are recorded. The regions from which the average values are taken are represented in grey in Figure S3. A line is fit to the resulting data, shown in Figure S4, at all five temperatures. The summary of the fits is shown in Table S1. The Y-intercept values represent a background "DC" heat flux into the sensor that needs to be appropriately adjusted, see Section S4.

Heat flux sensor temperature (K)	Slope ($\mu V/Wm^{-2}$)	Y-intercept (μV)
90	1.487(6)	58(1)
132	1.817(1)	58.6(3)
180	2.087(4)	64(1)
228	2.321(1)	46.8(4)
297	2.561(1)	-14.8(2)

TABLE S1. Fitting data from all calibration plots.

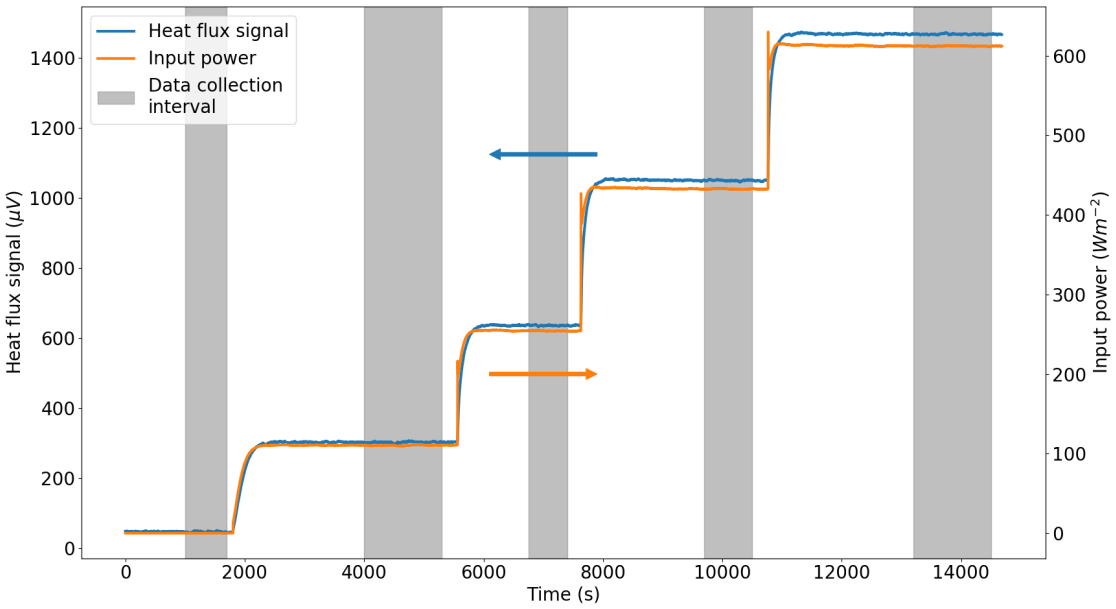

FIG. S3. **Representative plot of real time data for heat flux sensor calibration.** The heat flux voltage signal is measured for different input heating powers. After the signals have equilibrated, the data are collected and averaged over an allotted time interval, shown in grey.

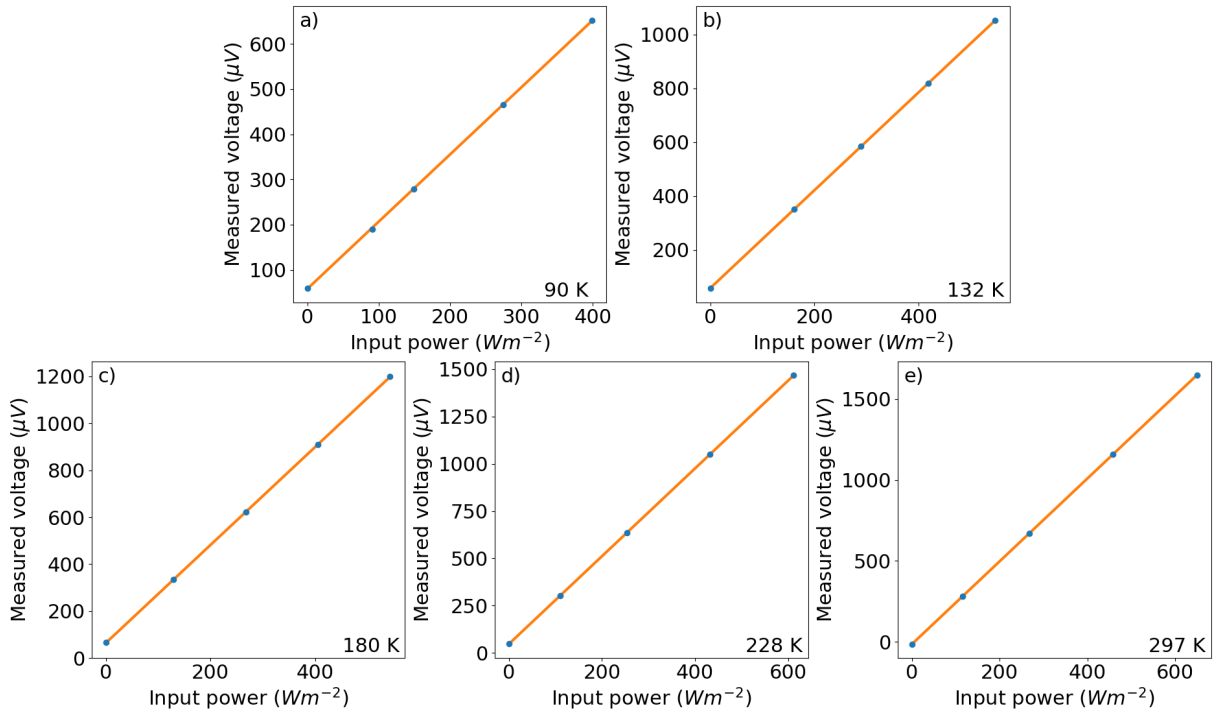

FIG. S4. **Calibration plots for heat flux sensor at different temperatures**. Each point represents the data averaged over a single grey interval in Figure S3. The inverse of the slope from each fitted line gives the conversion factor of measured voltage to input heat flux. The heat flux is normalized to the area of the heat flux sensor.

S4. BACKGROUND HEAT FLUX CORRECTION

The non-zero y-intercept values from the calibration fits indicate that there is a small background heat flux signal that must be addressed when converting the heat flux sensor voltage signal to a heat flux value. As shown in the diagram in Figures S5a and b, we divide this background "DC" heat flux into two pathways, one in which the heat flows directly into the sensor, and the other where the heat flows through the heater. As the entire assembly is radiation shielded, we attribute these small heat flows to heat leakage through connecting lead and thermocouple wires.

The heat that flows through the heater and into the sensor ultimately also flows through the sample itself and should *not* be subtracted from the heat flux signal. The heat that flows directly into the sensor, however, does not flow through the sample and should be subtracted. We carefully measure this background "DC" signal for two cases, where the heater is firmly pressed against the heat flux sensor and when the heater is suspended above the sensor. In the former case, heat flow pathways are open and are plotted in orange in Figure S6. In the latter case, heat cannot flow from the heater to the sensor (other than through a negligible far-field radiative pathway), and is plotted in blue in Figure S6.

Both curves show a monotonic decrease in background heat flow as the sensor temperature increases. The area beneath the blue curve represents the heat flowing directly into the sensor, and the area between the two curves, shown in orange, represents the heat only flowing through the heater. All heat flux modulation measurements are conducted where the cryostat cold finger is kept at 77 K, and the heat flux sensor is at 90 K. From these measurements, the background heat flux of 20 Wm^{-2}, area normalized to the heat flux sensor, is subtracted. This subtraction corresponds to a reduction in the heat flux sensor signal of 28 ± 5 μV. The uncertainty is mainly due to the signal drift of the heat flux sensor. As the temperature of the heat flux sensor asymptotically approaches its equilibrium value, so too does the heat flux sensor signal. This equilibration has been found to take many hours. Each data point in Figure S6 is collected after the sensor signal has flattened out, but the signal was found to continue to drift by close to 5 μV. This signal drift is also addressed in Section S5 for correcting the heat flux modulation measurement.

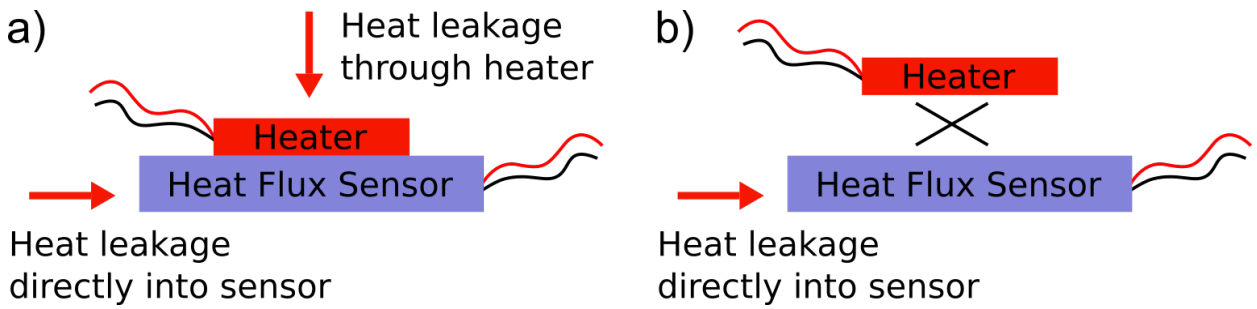

FIG. S5. **Diagram of thermal leakage pathways. a**, Heat flux sensor is pressed directly onto the heat flux sensor, allowing for two paths for heat to flow into the sensor, one direct and one indirect through the heater. **b**, The heater is elevated above the sensor, and only heat only flows into the sensor through directly. The heat that flows through the heater ultimately also flows through the sample, meaning that heat flow should *not* be subtracted from the end heat flux signal. Heat that flows directly into the sensor does not flow through the sample and should be subtracted.

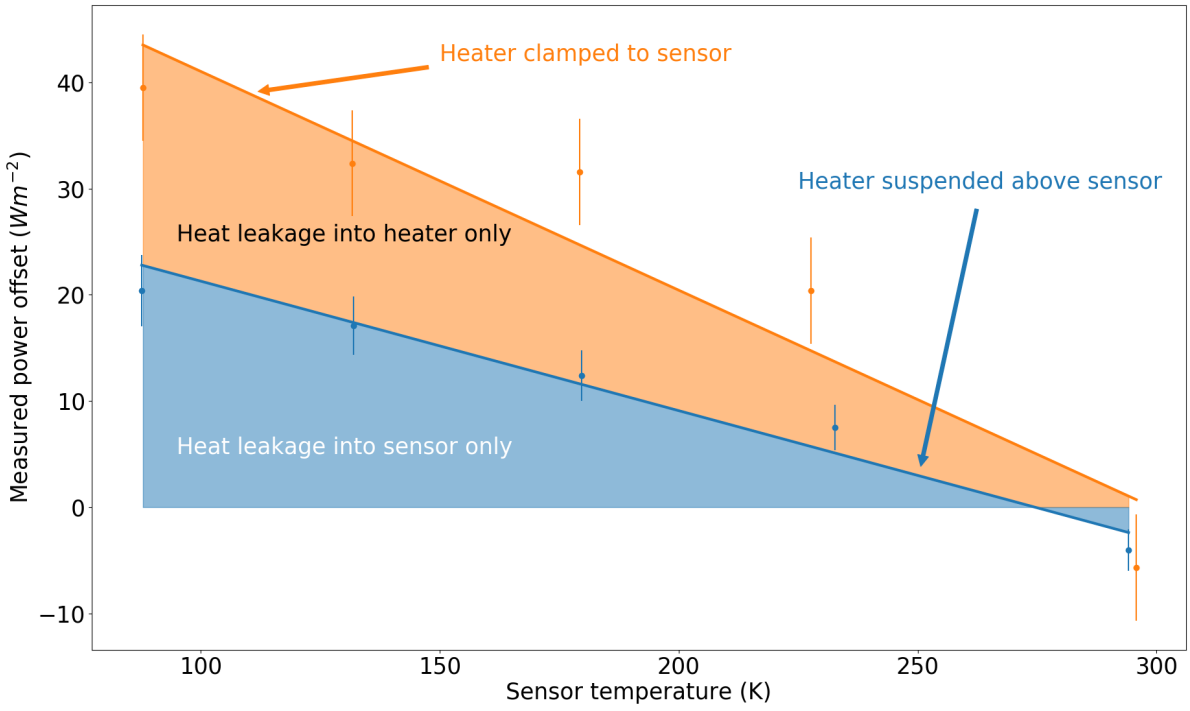

FIG. S6. **Background heat flux signal versus sensor temperature**. The measurements taken at zero input power from the resistive heater and are normalized to the area of the heat flux sensor.

S5. SIGNAL DRIFT

As mentioned in the previous section, the heat flux signal exhibits a linear drift (at the end of an asymptotic equilibration). To account for this drift, we fit a line to the raw heat flux signal at all times when zero bias is applied and then subtract off the slope×time, as shown in Figure S7. This effectively rotates the heat flux values down about time $t = 0$, and as a result reduces the absolute final heat flux values by 5 Wm^{-2}.

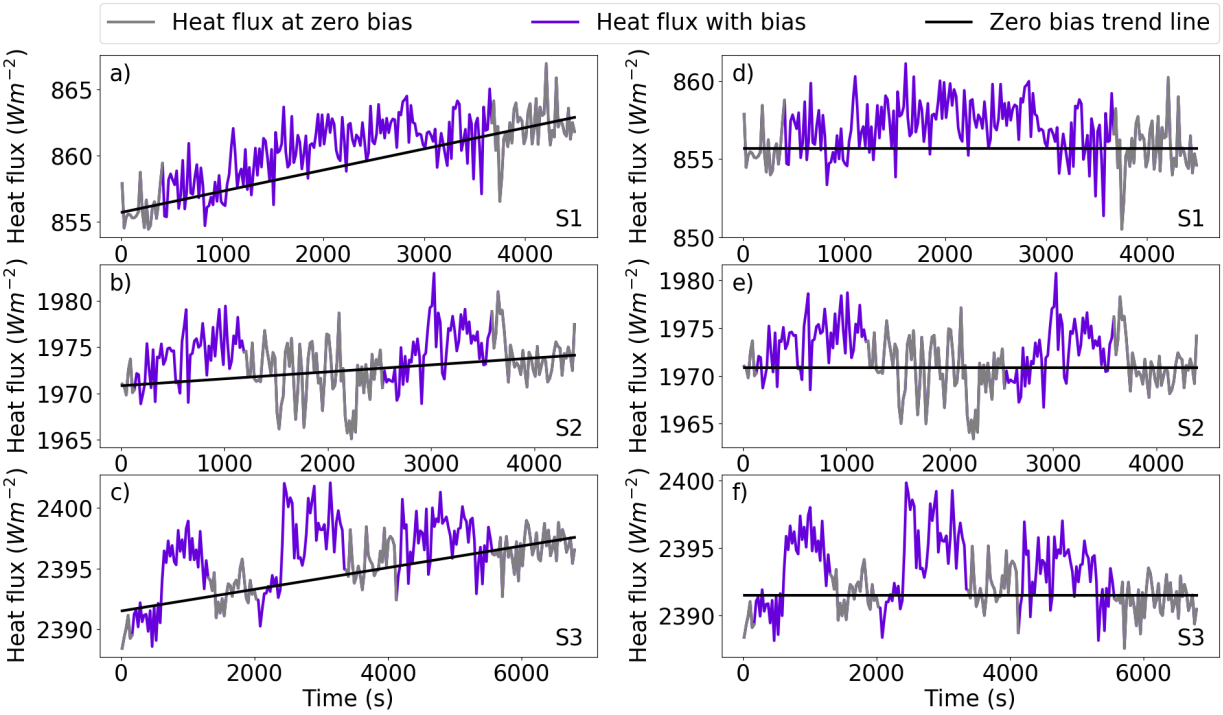

FIG. S7. **Signal drift correction for samples S1-S3.** The raw data are shown in **a-c**. A line is fit to the subset shown in gray at which zero bias is applied. The drift is removed by then subtracting off the slope×time from the entire data set. The result is in **d-f**.

S6. FITTING PROCEDURE FOR THERMAL MODEL

The radiative contribution to the heat flux is modeled in Equation S1

$$H(\omega, T_1, T_2) = \Phi(\omega)\left(\Theta(\omega, T_1) - \Theta(\omega, T_2)\right), \tag{S1}$$

where $\Phi(\omega)$ is the transmissivity function, partitioned over propagating modes where $k_{||} < \omega/c$, and evanescent modes where $k_{||} > \omega/c$,

$$\begin{aligned}\Phi(\omega) = &\sum_{s,p}\int_0^{\omega/c} dk_{||}\frac{k_{||}}{2\pi}\frac{(1-|r_{13}^{s,p}|^2)(1-|r_{23}^{s,p}|^2)}{|1-r_{13}^{s,p}r_{23}^{s,p}e^{i2k_{z0}d}|^2} \\ &+\int_{\omega/c}^{\infty} dk_{||}\frac{k_{||}}{2\pi}\frac{4\Im(r_{13}^{s,p})\Im(r_{23}^{s,p})}{|1-r_{13}^{s,p}r_{23}^{s,p}e^{-2|k_{z0}|d}|^2},\end{aligned} \tag{S2}$$

and the total integrated heat flux is

$$Q(T_1, T_2) = \int_0^{\infty}\frac{d\omega}{2\pi}H(\omega, T_1, T_2). \tag{S3}$$

The inherent dependence on Fermi levels is manifest in the Fresnel coefficients r_{13} and r_{23}. As there is considerable conductive leakage, we also account for an added conductive thermal pathway with an additional term proportional to $\Delta T = T_1 - T_2$,

$$Q_{total} = G(T_1 - T_2) + Q_{rad}\left(\mu, d, T_1, T_2\right). \tag{S4}$$

As the top and the bottom samples are in conductive contact, that likely means the top and bottom graphene sheets are also shorted electrically. As a result, the Fermi levels are assumed to be equal, $\mu_1 = \mu_2 = \mu$.

There are 5 parameters in the final model Equation S4. As shown in Section S1, the temperatures of the copper heat spreaders above and below the sample are tracked with thermocouples. To calculate the temperatures of each graphene surface, we employ a thermal resistor model, using the measured heat flux. As thermal grease is applied to each heat spreader, the interfacial resistance is negligible compared to the thermal resistance between the two graphene sheets [2]. As the thermal conductivity of the bottom silicon wafer is comparatively high, the bottom graphene temperature T_2 is approximately equal to the measured temperature of the heat flux sensor. However, as the thermal conductivity of the silica optical flat is comparatively low, there is a temperature drop from the resistive heater to the top graphene surface T_1, proportional to the thermal conductivity of silica.

The heat transfer coefficient G, the Fermi levels, and the gap spacing can be determined in the following manner. The Fermi levels can be determined by finding the charge neutral point at maximum surface resistance, and then using a capacitor model to solve for Fermi level as a function of applied voltage, shown in Figure S9d-f for samples S1, S2, and S3, respectively. Once the Fermi levels are established, the absolute change in heat flux ΔQ_{rad} is only a function of vacuum gap spacing d. As a result, from the measured heat flux change, we uniquely determine the value for d as shown in Figure S8. G is then found to account for the heat flux discrepency between Q_{total} and Q_{rad}. This discrepancy was found to be 731 $\pm$ 9, 1590 $\pm$ 30, and 2011 $\pm$ 20 Wm^{-2} for samples S1-S3, respectively, indicating that parasitic conduction is responsible for 85 $\pm$ 1, 81 $\pm$ 1, and 84.1 $\pm$ 0.6 %, respectively, of the total heat flux. The final parameter values for are tabulated in Table S3. Uncertainties are determined in SI Sec. S7.

As the top sample consists of an optical flat and graphene, it is transparent to visible light and we can set upper limits on the gap spacing using interferometry, shown for samples S1 through S3 in Figure S9 and tabulated for different points on each sample in Table S2. The estimated distance is quite variable for S1, indicating that there is likely a piece of dust beneath the optical flat, causing it to be cantilevered. For S3 the spacings are uniform and close to the distance that gives the appropriate level of heat flux modulation. However, for S2 the measure gap is about 1 μm larger than expected. During the heat flux measurement, the spring-loaded heater presses the optical flat to the underlying substrate, and in an analogous experiment by simply pressing on the sample with tweezers, applying pressure was found to reduce the spacing by upwards of 50%, as shown for Sample S4 in Figure S10. As a result, the gap spacing measurements only provide an upper limit on the gap spacing at a particular point on the sample since the spacing is highly dependent on applied pressure.

The fitting procedure is modified for the sample S4, since the charge neutral point could not be found under forward bias as dielectric breakdown occurred at smaller biases than for the previous samples. Therefore the zero-bias Fermi level is also a fitting parameter where the previous three samples provide an approximate range for the charge neutral point. The three parameters G, d, and μ are found in the zero-bias case, and then a zero-parameter fit is applied to the biased case with the corrected Fermi level.

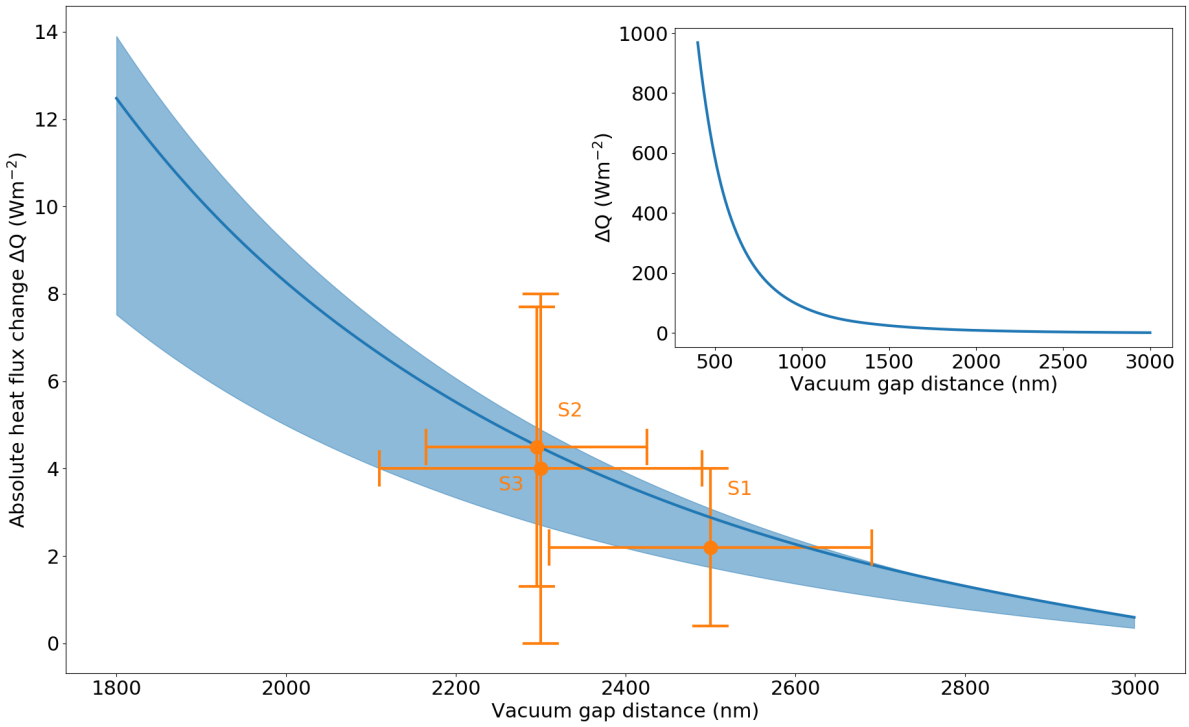

FIG. S8. **Heat flux change due to Fermi level change versus vacuum gap distance**. The Fermi level sweeps between 0.05 eV to 0.30 eV (blue line), where the shaded region outlines the heat flux change accounting for the uncertainty in the Fermi level of ±0.05 eV. The vertical error bars for each sample indicate the uncertainty in heat flux measurement, and the horizontal error bars indicate the uncertainty in the solved distance d. The inset shows the heat flux change at distances from 400 nm to 3 μm.

Measurement Location	S1	S2	S3	S4
#1	5.63 μm	3.20 μm	2.46 μm	1.43 μm
#2	1.28 μm	4.08 μm	2.70 μm	0.65 μm*
#3	3.74 μm	3.45 μm	2.31 μm	

TABLE S2. Vacuum gap distances for each sample. The sample S1-3, the interferometric measurements were taken at different locations around the optical flat. For sample S4, the samples were taken when pressure was applied (indicated by the *), and when no pressure was applied.

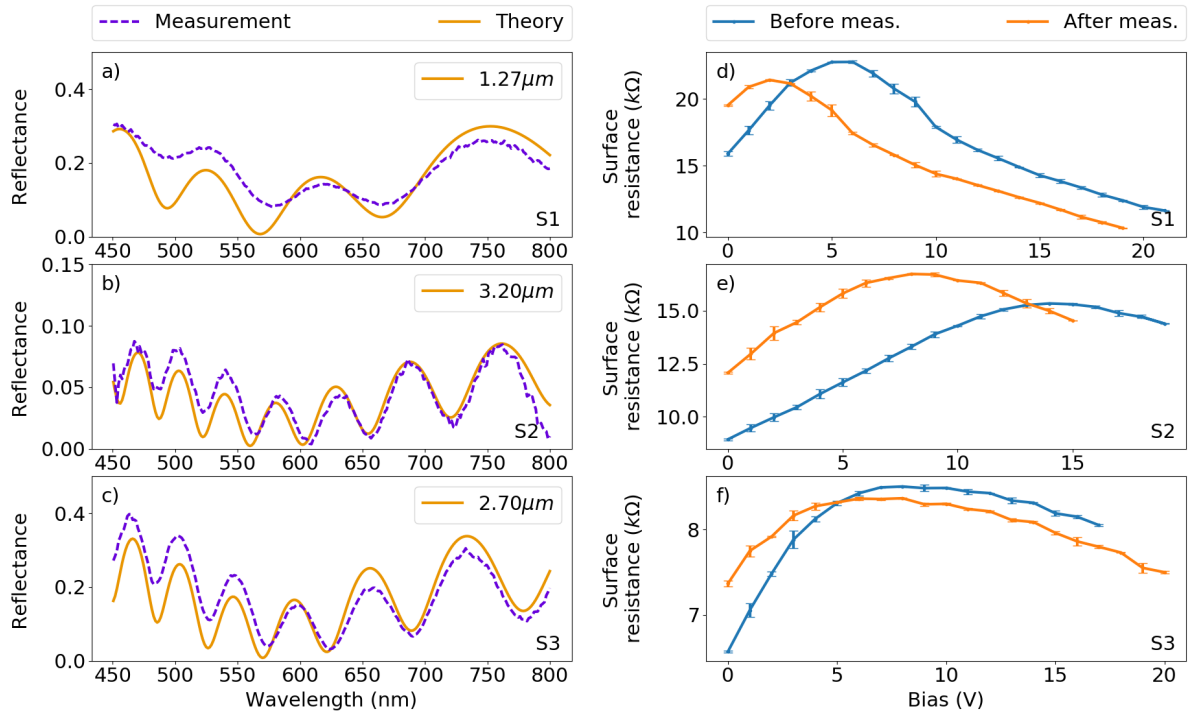

FIG. S9. **Measurements for model parameters. a-c**, Measurements for sample gap spacing for S1-S3, respectively. A transfer matrix model with a variable gap spacing and amplitude is fit to the measured signal. **d-f**, Graphene surface resistance versus applied bias for S1-S3, respectively. The peak in the surface resistance measurement is the charge neutral point where the graphene Fermi level is near zero.

	S1	S2	S3	S4
G ($\mathrm{Wm^{-2}K^{-1}}$)	6.59	8.88	11.20	5.10
d (μm)	2.5	2.3	2.3	0.56
T_1 (K)	197	270	269	-
T_2 (K)	86	91	90	-
CNP (V)	5	15	7	-

TABLE S3. Parameters for the model in Equation S4. The values G and d are fit to heat flux data. The temperatures are taken from measurement, accounting for the thermal resistance of the optical flat. The charge neutral point (CNP) is the voltage at which the graphene surface resistance is maximized and the Fermi level is near zero.

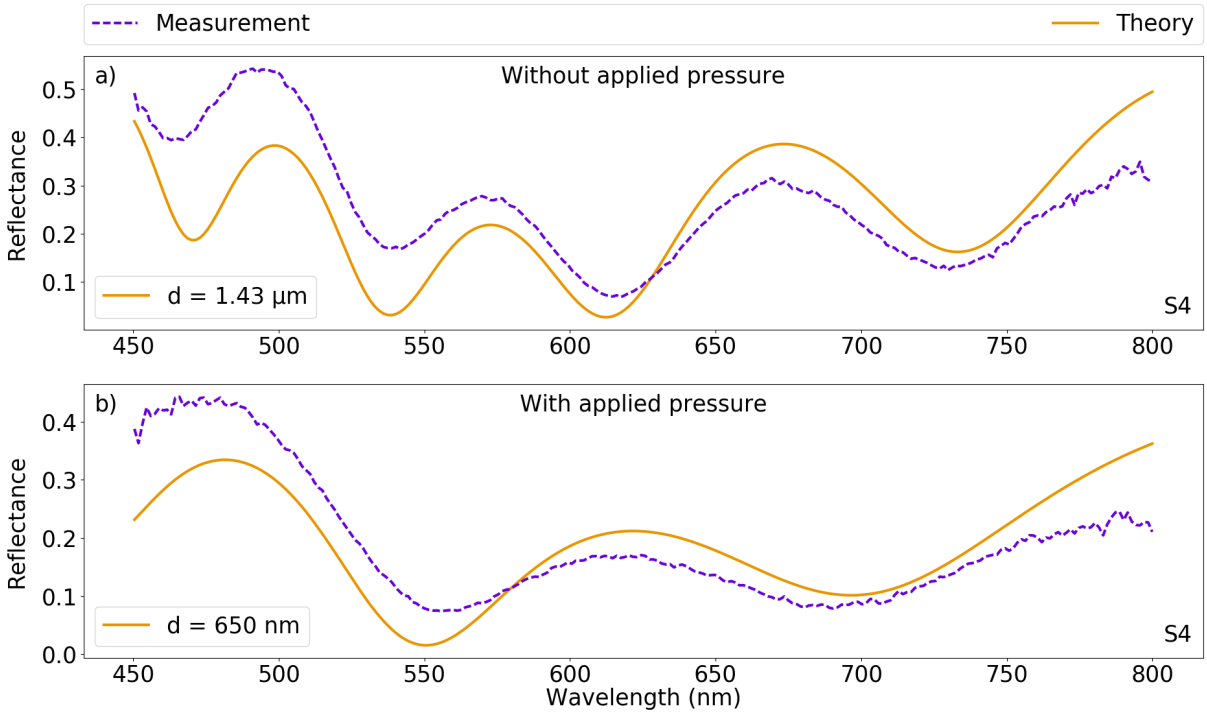

FIG. S10. **Interferometic measurments for S4. a**, Without applied pressure. **b**, With applied pressure. By pressing down on the optical flat during measurement, the gap spacing decreases by over 50%. As the sample is compressed during the heat flux measurements and the interferometric measurements are taken without such added pressure, the measured values of d in Table S2 serve as an upper bound.

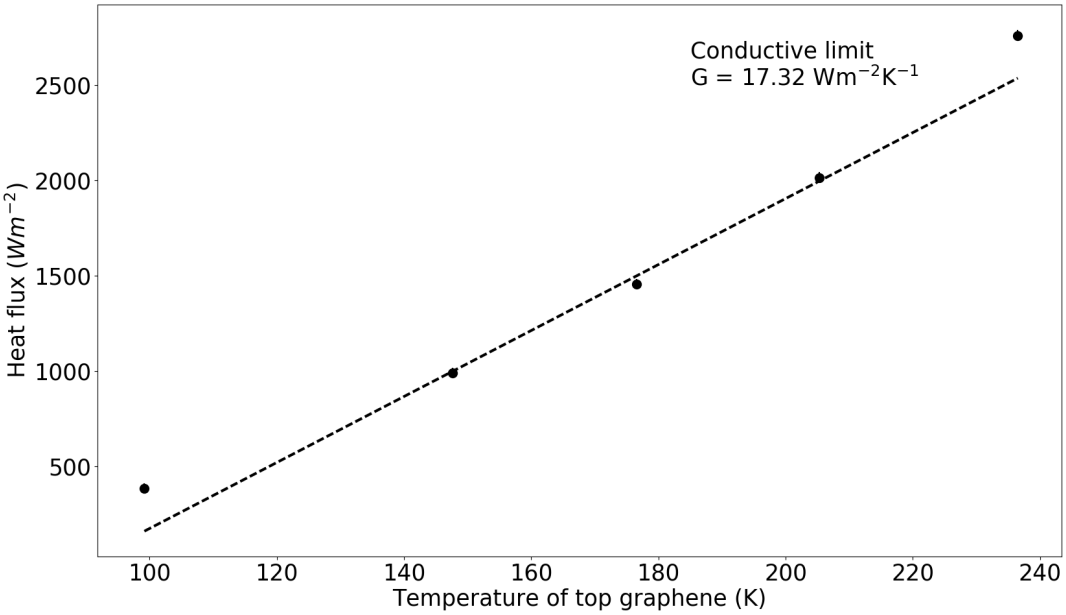

FIG. S11. **Heat flux versus temperature on sample without SiO_2 spacers.** The upper limit of the heat transfer coefficient for the samples studied here is $\sim$17 $\mathrm{Wm^{-2}K^{-1}}$.

S7. SIGNAL TO NOISE & STATISTICAL UNCERTAINTY

To estimate the ratio of signal to noise, we isolate the parts of the data that constitute the heat flux baseline at zero bias and the heat flux signal while under bias, shown in Figure S12a-c. The heat flux data under bias are collected after the signal has equilibrated up until the start of the voltage ramp back to zero. The data for the third voltage cycle of sample S3 are not included as the dielectric has started to break down. For each interval, we plot the signal to noise ratio in Figure S12d:

$$SNR = \frac{\overline{HF(-100\ V)} - \overline{HF(0\ V)}}{\sqrt{\sigma^2_{HF(-100\ V)} + \sigma^2_{HF(0\ V)}}}, \tag{S5}$$

In all cases, the signal to noise ratio is greater than one, indicating the heat flux modulation depth is greater than one standard deviation.

Having established the uncertainty in the measured heat flux change for each sample, $\sigma_{\Delta Q} = \sqrt{\sigma^2_{HF(-100\ V)} + \sigma^2_{HF(0\ V)}}$, we can further propagate errors to estimate the uncertainty in the fitted vacuum gap distance d. As stated in Section S6, the radiative heat flux Q_{rad} is a function of four variables, d, μ, T_1, T_2. The measured heat flux change ΔQ due to the applied bias is

$$\Delta Q = Q_{rad}(d, \mu_1, T_1, T_2) - Q_{rad}(d, \mu_2, T_1, T_2), \tag{S6}$$

where μ_1 and μ_2 are the Fermi levels for the sample under a bias of -100 V and under zero bias, respectively. The uncertainty in the heat flux change $\sigma_{\Delta Q_{rad}}$ is therefore

$$\sigma_{\Delta Q_{rad}} = \sqrt{\sum_n \left(\frac{\partial \Delta Q_{rad}}{\partial n}\right)^2 \sigma_n^2}, \tag{S7}$$

where $n \in [d, \mu_1, \mu_2, T_1, T_2]$. Therefore, the uncertainty in the vacuum distance is

$$\sigma_d = \sqrt{\frac{\sigma^2_{\Delta Q_{rad}} - \sum_{n \neq d} \left(\frac{\partial \Delta Q_{rad}}{\partial n}\right)^2 \sigma_n^2}{\left(\frac{\partial \Delta Q_{rad}}{\partial d}\right)^2}}. \tag{S8}$$

As the transmissivity function Φ is only weakly dependent on temperature, we can approximate the partial derivative with respect to temperature as

$$\left(\frac{\partial \Delta Q_{rad}}{\partial T_{1,2}}\right)^2 = \left(\int \frac{\omega}{2\pi} \frac{\partial \Theta(T,\omega)}{\partial T}\Big|_{T_1,T_2} [\Phi(\omega, \mu_1, d) - \Phi(\omega, \mu_2, d)] \right)^2 \tag{S9}$$

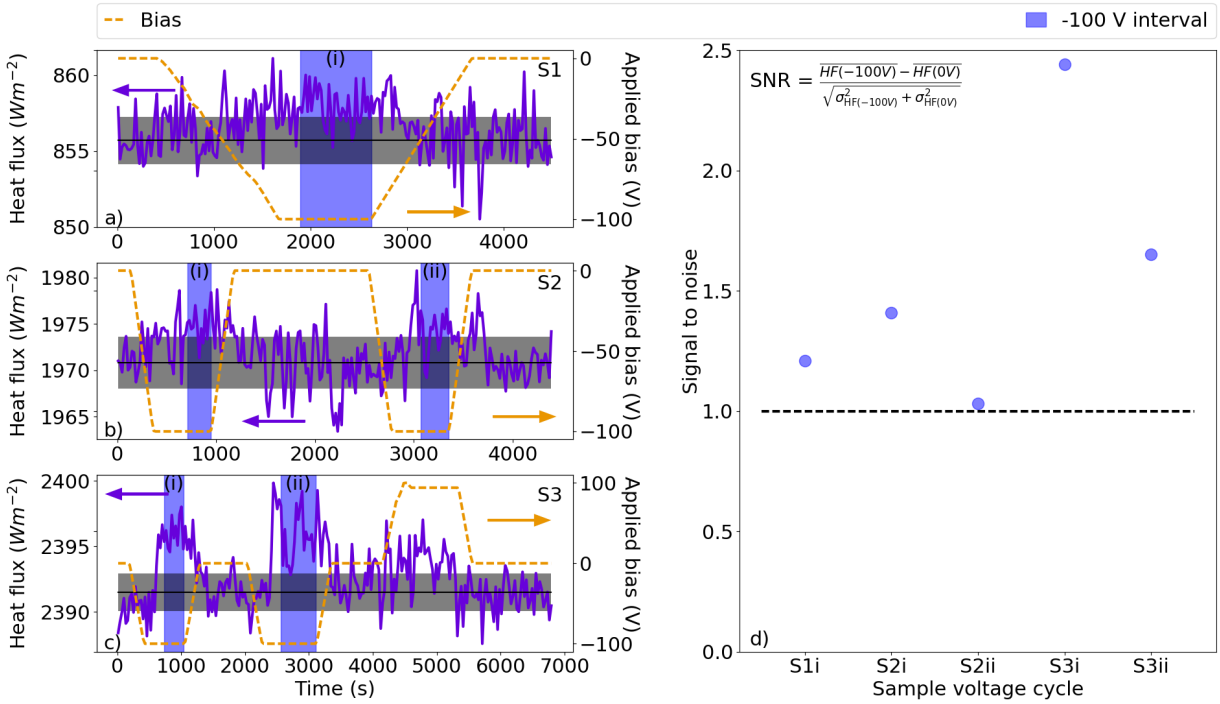

FIG. S12. **Signal to noise ratio for each sample and voltage cycle**. **a - c**, Heat flux measurements under bias for samples S1-S3, respectively. The collected signal data are indicated in the blue intervals. The zero bias baseline is shown in grey. As S3 begins to breakdown during the third voltage cycle, that cycle is not included in this analysis. **d**, The signal to noise ratio for the 5 collection intervals.

The other partial derivatives we compute numerically from a 2-D lookup table generated with Equations S1, S2, and S3. The uncertainty in each of the Fermi levels, σ_{μ_1} and σ_{μ_2}, is 0.05 eV, and the uncertainty in each of the temperature values T_1 and T_2 is 2 K. Computing each of these partial derivatives numerically, we get the uncertainty in the distance values d, shown in Table S4.

	S1i	S2i	S2ii	S3i	S3ii
d (μm)	2.5	2.3	2.3	2.3	2.3
σ_d (nm)	190	130	190	80	130

TABLE S4. Vacuum gap distance and uncertainty for each sample and each voltage cycle. The final cycle for S3 is excluded as the dielectric has started to break down.

With these distance uncertainties, we can further conduct error propagation in the esti-

mate of the purely radiative component of the heat flux, Q_{rad}. The values for Q_{rad} and the ratio to the black body limit are tabulated in Table S5.

	S1	S2	S3
Q_{rad} (Wm^{-2})	125 ± 9	385 ± 26	381 ± 18
BB limit (Wm^{-2})	84 ± 4	299 ± 9	295 ± 9
Ratio Q_{rad} to BB	1.5 ± 0.1	1.29 ± 0.07	1.29 ± 0.09

TABLE S5. Radiative contribution to heat flux. The radiative contribution to heat flux exceeds the blackbody limit, indicating near field optical coupling between the top and bottom of the graphene heterostructures.

S8. LEAKAGE CURRENT

Leakage current through the gate dielectric during biases poses a potential problem for heat flux measurements. High leakage currents would cause non-negligible Joule heating of the sample and register as additional heat flux. Therefore, careful preparation of the samples and maintaining the biased sample as close to 77 K as possible to keep leakage currents low is required. In all measurements, leakage current is recorded with applied bias, allowing for direct calculation of the injected heat, which is subtracted from the final heat flux signal. Accurately accounting for offset of the potential injected heat requires the careful heat flux sensor calibration discussed in Section S3.

Although the injected heat is accounted for, we demonstrate it has negligible effect. Shown in Figure S13 are the leakage power data over time mapped over the raw heat flux signal (orange) and the heat flux adjusted for injected power (blue) for sample S3. In the final case, where the leakage power jumps, the sample was biased to $+95\ V$, whereas in the previous two cases the sample was biased to $-100\ V$. Although the injected leakage power is 20 times greater for the final case, the measured change in heat flux is nearly identical to the -100 V bias cases, indicating the injected Joule heat is not the origin for the heat flux change.

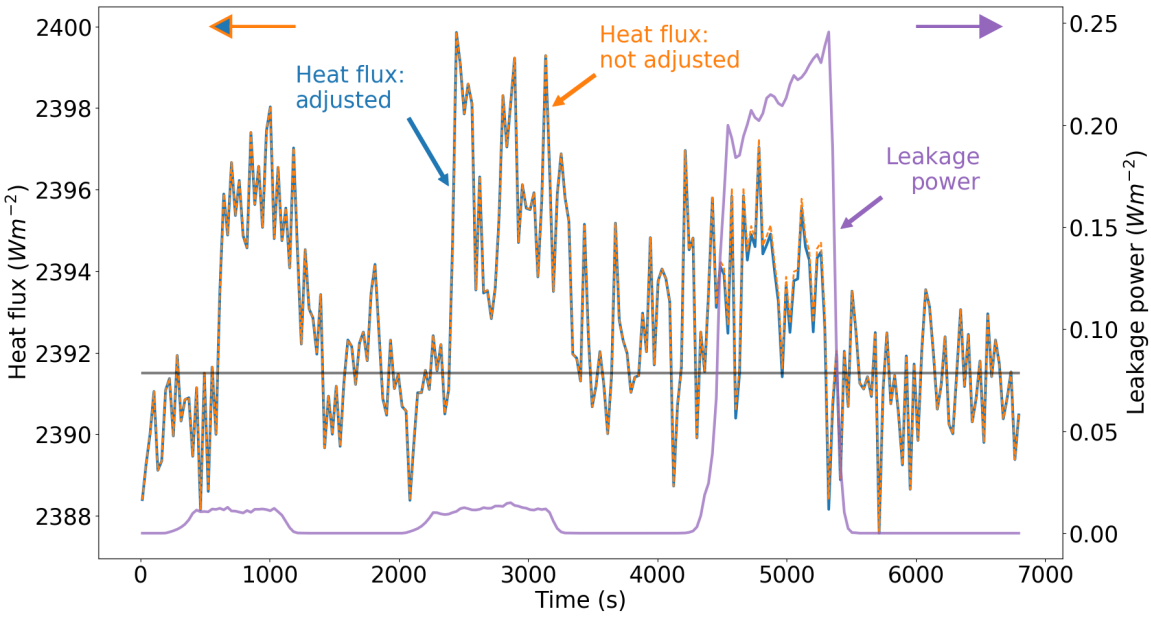

FIG. S13. **Leakage power and heat flux for S3 versus time**. The adjusted heat flux is the difference between the not-adjusted heat flux signal and the leakage power. The final jump in leakage power corresponds to when the sample was forward biased to 95 V. In this case, the leakage power is 20 times larger than the previous -100 V cases, however the change in heat flux is not significantly different considering the signal noise.

S9. OPTICAL PROPERTIES

The permittivity values used in simulation were taken from analytical formulations [1, 3, 4]. The optical properties are shown in Figure S14a and b for SiO_2 and Al_2O_3, respectively.

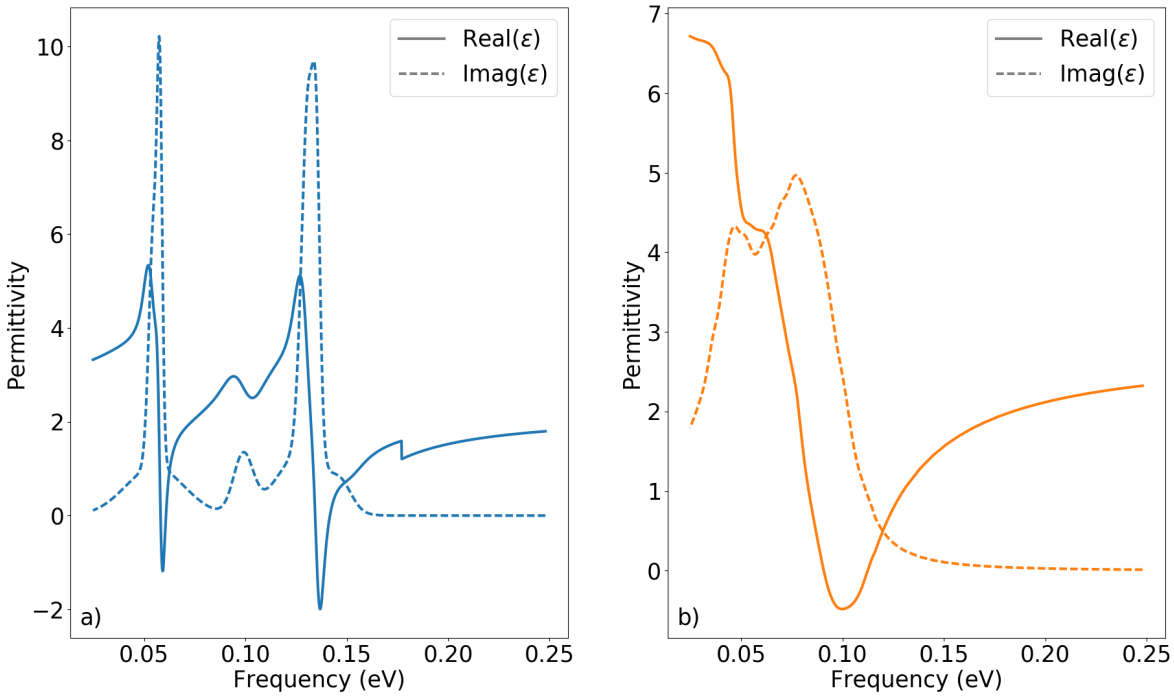

FIG. S14. **Material permittivities versus frequency**. **a**, SiO_2 (blue) and **b**, Al_2O_3 (orange).

[1] T. S. Eriksson, A. Hjortsberg, G. A. Niklasson, and C. G. Granqvist. Infrared optical properties of evaporated alumina films. *Appl. Opt.*, 20(15):2742–2746, August 1981.

[2] Kota Ito, Atsushi Miura, Hideo Iizuka, and Hiroshi Toshiyoshi. Parallel-plate submicron gap formed by micromachined low-density pillars for near-field radiative heat transfer. *Appl. Phys. Lett.*, 106(8):083504, 2015.

[3] Jan Kischkat, Sven Peters, Bernd Gruska, Mykhaylo Semtsiv, Mikaela Chashnikova, Matthias Klinkmller, Oliana Fedosenko, Stephan Machulik, Anna Aleksandrova, Gregorii Monastyrskyi, Yuri Flores, and W. Ted Masselink. Mid-infrared optical properties of thin films of aluminum

oxide, titanium dioxide, silicon dioxide, aluminum nitride, and silicon nitride. *Appl. Opt.*, 51 (28):6789–6798, October 2012.

[4] Rei Kitamura, Laurent Pilon, and Miroslaw Jonasz. Optical constants of silica glass from extreme ultraviolet to far infrared at near room temperature. *Appl. Opt.*, 46(33):8118–8133, November 2007.